Arabian Journal for Science and Engineering (2023) 48:953–966
https://doi.org/10.1007/s13369-022-07241-2

RESEARCH ARTICLE-PHYSICS

Transportation of Hybrid MoS_2–SiO_2/EG Nanofluidic System Toward Radially Stretched Surface

Iftikhar Ahmad[1] · Syed Ibrar Hussain[2] · Muhammad Asif Zahoor Raja[3] · Muhammad Shoaib[4] · Qurratulain[1]

Received: 1 May 2022 / Accepted: 24 August 2022 / Published online: 19 September 2022

Abstract

A stochastic computing approach is implemented in the present work to solve the nonlinear nanofluidics system that occurs in the model of atomic physics. The process converts the partial differential nanofluidics system with suitable level of similarities transformation into nonlinear systems of differential equations. For the construction of datasets, finite difference scheme (Lobatto IIIA) is applied through different selection of collocation points for nonlinear nanofluidics system having accuracy of order four. Lobatto IIIA has a strong point to tackle extremely nonlinear systems of ordinary differential equations in smooth way. For different scenarios, datasets are well trained through computing scheme to investigate the heat transfer and thermal performance of nanofluidic transportation system of nanofluids and hybrid nanofluids toward stretching surfaces with variation of Biot number, Nusselt number and skin fraction. Furthermore, the reliability, accuracy and efficiency are endorsed through various statistical analysis and graphical illustrations of proposed computing scheme.

Keywords Nanofluidic system · Stochastic computing · Finite difference technique · Biot number · Skin friction

List of Symbols

λ	Heat generation parameter
M	Hartman number
Bi	Biot number
Pr	Prandtl number
$\mathrm{Nu}_{\bar{r}}$	Local Nusselt number
C_{f}	Skin friction coefficient
k	Thermal conductivity
c_p	Specific heat
ϕ_1 & ϕ_2	Volumetric fractions
μ_{hnf}	Dynamic viscosity
ρ_{hnf}	Density of hybrid nanofluid
σ_{hnf}	Electrical conductivity of hybrid nanofluid
$f_{\mathrm{w}}(\bar{r})$	Injection/suction velocity
$U_{\mathrm{w}}(\bar{r})$	Uniform velocity
T_∞	Ambient temperature
h_{f}	Heat transfer coefficient

✉ Syed Ibrar Hussain
syedibrar.hussain@unipa.it

Iftikhar Ahmad
dr.iftikhar@uog.edu.pk

Muhammad Asif Zahoor Raja
rajamaz@yuntech.edu.tw

Muhammad Shoaib
dr.shoaib@cuiatk.edu.pk

Qurratulain
qurratulain533@gmail.com

[1] Department of Mathematics, University of Gujrat, Gujrat 50700, Pakistan

[2] Department of Mathematics and Computer Science, University of Palermo, Via Archirafi 34, 90123 Palermo, Italy

[3] Future Technology Research Center, National Yunlin University of Science and Technology, 123 University Road, Section 3, Douliou, Yunlin 64002, Taiwan

[4] Department of Mathematics, COMSATS University Islamabad, Attock Campus, Attock 43600, Pakistan

1 Introduction

Several base fluids like water, glycol and alcohol have rather low viscosity, thermal conductivity and may not be used independently in several applications, the suspension containing nanoparticles combined with the base fluid [1]. A special type of fluid known as nanofluid has been introduced, to overcome this weakness. Due to the extreme essential properties of heat transfer, such nanofluids are commonly used for macroscopic cooling [2]. In everyday life, implementations such as portable computer processors, lubricant processing, coolants, air conditioning, freezers and nanotechnology, the

single-phase flow model of nanofluids is of considerable significance [3]. Narla et al. have presented the pumping of electroosmotic nanofluid past a curved channel [4]. A very simple and environment friendly conversion method of ultraviolet irradiance to heat energy is identified as a solar collector, used in the industrial sector [5]. In such collectors, different fluids like water and glycol are being used to improve their power and performance [7]. Sheikholeslami et al. have analyzed the hydrothermal analysis of nanofluids with wavy pipe absorber [6]. Recently, both numerically and experimentally, Li et al. [8] have presented the use of nanofluids in certain kinds of solar collectors. Oke [9] has discussed and numerically analyzed a special type of nanofluid known as gold-water nanofluid and presented the obtained results.

There is another classification of nanofluids obtained by dispersing two or more types of nanoparticles in conventional fluid, termed as hybrid nanofluids [10]. Hybrid nanofluids are essential because they are potential heat transfer fluids that possess more enhanced thermophysical properties and better thermal performance than base fluids and nanofluids having single type of nanoparticles [11]. Algehyne et al. [12] have presented the BVP of Maxwell hybrid nanofluid and its thermophysical performances. Khan et al. [13] have investigated a fractional model on hybrid nanofluids with porous medium. The use of nanoparticles for imaging and sensing purposes in bio-medical field has become very important for advance applications [12]. This growth in the field of nanoparticles is directly linked with designing new materials at nanoscale level along with innovations in imaging technologies to measure and manipulate nanomaterials [14]. The ternary MHD hybrid nanofluid flow past a rotating surface is treated numerically by Oke [15]. The production, usage and disposal of synthesized nanoparticles will cause expulsion of air, sand, soil and water systems. Harmful effects are to be expected; therefore, minimization and quantification of these negative effects on ecological health are of great importance [16]. Therefore, true information about chemical and physical properties of nanoparticles in consideration of realistic circumstances is necessary to predict their toxicity, fate and behavior in normal aquatic environment [17].

The phrase thin film is widely used to describe flow that is defined by the thickness of a layer of material ranging from nanometer scale to the several micrometers. In one dimension (one or two dimensions), the flow spectra are significantly less than the other [18]. It is a property that may be utilized to simplify Navier–Stokes equations [19]. The structural importance of flow problems with thin films (flow) is significant [20]. Thin-film flow problems in regular activities range from simple to sophisticated effects, such as transmitting a rain drop on an airplane window [21]. Siddiqui et al. [22] implemented the He's homotopy method for third-grade TFF fluid flow. It is true that thin-film flow is used in a variety of industrial processes [23]. The Casson hybrid nanofluid based on TFF is analyzed by Alhussain and Tassaddiq [24]. Researchers are interested in working on this topic because of its extensive applications in sectors such as coating material, industrial processes, chemical engineering, cooling and the lubrication of thermal changer fins into contact lens motion, dam breaking wave simulation and nuclear reactor fluid dynamics that are among the most significant industrial applications [25]. The TFF flow past a stretching sheet is numerically tackled by Kamis et al. [26]. The representation of TFF dynamics is similar to tear films in the eye and membranes in the biophysics field [27]. The most prevalent fluid properties are thin-film flow and flow characteristics. Furthermore, in this advanced and fast-paced era, thin film allows all those involved to monitor the output of paints in surface flow coverings, plan the layout of nuclear reactors and reduce the structure of equipment such as lubricating fluid [28]. TFF's biological uses are similar to red blood cells flowing via veins, eyes and lungs [18]. A neuro-heuristic intelligent algorithm is utilized by Ahmad et al. [29] to evaluate TFF model.

Many engineering systems involving electro-magnetic accelerators and magnetohydrodynamic (MHD) power generators work on high temperatures; therefore, the understanding of MHD nanofluidic flow past has become very essential in production of appropriate equipment [31]. Thus, problems regarding nanofluids and magnetohydrodynamics (MHD) have become mechanically more important [32]. The modified Eyring Powell MHD fluid flow is presented and numerically solved by Oke [33]. The concept of using nanofluids in magnetohydrodynamic (MHD) flows over different flow geometries (specifically stretching sheets) has been presented due to the stability, enhanced heat transfer and effective thermal conductivity of these kinds of fluids [34]. Thermal conductivity of the nanofluids contributes in better performance, high energy proficiency and subordinate operating costs, discussed by Ijaz and Ayub in [35].

Lobatto IIIA based on finite difference method is a version of bvp4c method. The numerical code bvp4c in MATLAB, which is a finite difference technique, implements the 3-stage Lobatto IIIA formula that is a collocation technique having accuracy of order four. In the literature usually, the symbol III is associated with Lobatto methods because symbols I and II are held in reserve for two kinds of Radau methods [36]. A collocation method based on Lobatto IIIA technique is utilized by Oke et al. [37] for numerical solution of transformed ordinary differential equations. Lobatto IIIA method has a strong point to tackle extremely nonlinear systems of ordinary differential equations (ODEs) [38]. Implementation of Lobatto IIIA method to attain better approximation and rapid convergence is an inventive effort, used by Ahmad et al. [39].

The salient features of the proposed techniques are itemized as follows:

- A novel investigation is presented to examine the heat transfer and thermal performance of nanofluidic transportation of nanofluids and hybrid nanofluids toward stretching surfaces by Lobatto IIIA techniques.
- The governing physical flow systems are modeled mathematically in curvilinear coordinates and simplified by using appropriate transformations.
- The simplified systems of nonlinear differential equations are numerically treated to investigate the influences of emerged physical parameters on temperature, pressure and velocity profiles.
- A comparative dynamical analysis of nanofluids and hybrid nanofluids under the influence of emerging parameters is presented through tables and graphs which ascertain the worth of the scheme as an effective and viable computing solver.
- The conceptual simplicity, smoothness and stability are the hallmarks of the proposed study.

The framework of rest of the manuscript is structured as follows: Mathematical development and modeling of the problems is provided in Section two, results obtained by computational technique are presented graphically as well as in tabulated form in Section three, while the Section four includes the conclusion and future research study.

2 Mathematical Development

This section is held in reserve to the mathematical development and numerical simulation of axisymmetric flow of SiO_2/EG-based nanofluid and hybrid MoS_2–SiO_2/EG-based nanofluid on a radially stretched surface under consideration of magnetic field effect along with the internal heat absorption/generation. Lobatto IIIA is employed for computational exploration of governing flow model. Here ethylene glycol is taken as base fluid, molybdenum sulfide (MoS_2) and silicon dioxide (SiO_2) as ultra-fine nanoparticles. Hybrid nanofluid is prepared by inserting the nanoparticles of MoS_2 and SiO_2 in ethylene glycol.

2.1 Mathematical Modeling

A porous infinite radially stretched disk is considered for electrically conducting and incompressible nanofluidic flow. This opted disk is placed at the plane where $\bar{z} = 0$. Nanocomposite MoS_2–SiO_2/EG fluid flow is taking place above a half space $\bar{z} > 0$. This hybrid nanofluidic mixture contains 1% of SiO_2 volumetric fraction (ϕ_1), while MoS_2 volumetric fraction (ϕ_2) varies from 1 up to 5%. Equation (1) determines the nanoparticles volumetric fraction ϕ_{hnf} of the hybrid MoS_2–SiO_2/EG nanofluid.

$$\phi_{\text{hnf}} = \frac{V_{MoS_2} + V_{SiO_2}}{V_{\text{total}}} = \phi_1 + \phi_2. \tag{1}$$

Magnetic field B_0 having uniform intensity is applied in axial direction, and magnetic induction is unnoticed assuming the sufficiently weak magnetic field. The current analysis is done in cylindrical coordinates $(\bar{r}, \bar{\theta}, \bar{z})$. Moreover, the flow is generated due to the reason of stretching of the surface along radial direction. This flow has uniform velocity $U_{\text{w}}(\bar{r}) = c\bar{r}$, where real number c is nonnegative. Surface of the porous disk is incorporated with heat transfer along with internal heat generation. Furthermore, lower surface is assumed to be heated through convection using a warm fluid having temperature T_{f}. Temperature T_{f} is more than that of constant ambient temperature T_∞ and gives a heat-transfer coefficient h_{f}. The physical structure of governing flow model is demonstrated in Fig. 1.

The derivatives regarding $\bar{\theta}$ are absent because of axial symmetry of the leading engineering problem. Using above considerations together with boundary-layer approximations, the principal equations can be coupled into the subsequent forms.

$$\frac{\partial u}{\partial \bar{r}} + \frac{u}{\bar{r}} + \frac{\partial w}{\partial \bar{z}} = 0, \tag{2}$$

$$u\frac{\partial u}{\partial \bar{r}} + w\frac{\partial u}{\partial \bar{z}} = \frac{\mu_{\text{hnf}}}{\rho_{\text{hnf}}}\frac{\partial^2 u}{\partial \bar{z}^2} - \frac{\sigma_{\text{hnf}}^2 \beta^2}{\rho_{\text{hnf}}}u, \tag{3}$$

$$u\frac{\partial T}{\partial \bar{r}} + w\frac{\partial T}{\partial \bar{z}} = \alpha_{\text{hnf}}\frac{\partial^2 T}{\partial \bar{z}^2} + \frac{Q}{\left(\rho c_p\right)_{\text{hnf}}}\left[T - T_\infty\right]. \tag{4}$$

along with related boundary conditions

$$\begin{aligned} &u = U_{\text{w}}(\bar{r}) = c\bar{r},\ w = -f_{\text{w}}(\bar{r}), \\ &-k_{\text{hnf}}\frac{\partial T}{\partial \bar{z}} = h_{\text{f}}\left(T_{\text{f}} - T\right),\ \text{at } \bar{z} = 0, \end{aligned}$$

$$u \to 0,\ T \to T_\infty \text{ as } \bar{z} \to \infty. \tag{5}$$

where u and w are components of velocity along $\bar{r}$ and $\bar{z}$-axis, correspondingly. Furthermore, μ_{hnf}, ρ_{hnf} and σ_{hnf} indicate hybrid nanofluidic dynamic viscosity, density and electrical conductivity, respectively. $f_{\text{w}}(\bar{r})$ is injection/suction velocity over the radial disk's surface.

2.2 Numerical Simulation of Model

Numerical exploration of temperature and velocity profiles for the hybrid MoS_2–SiO_2/EG nanofluidic flow over a porous infinite radially stretched surface is done by employing Lobatto IIIA technique according to process illuminated

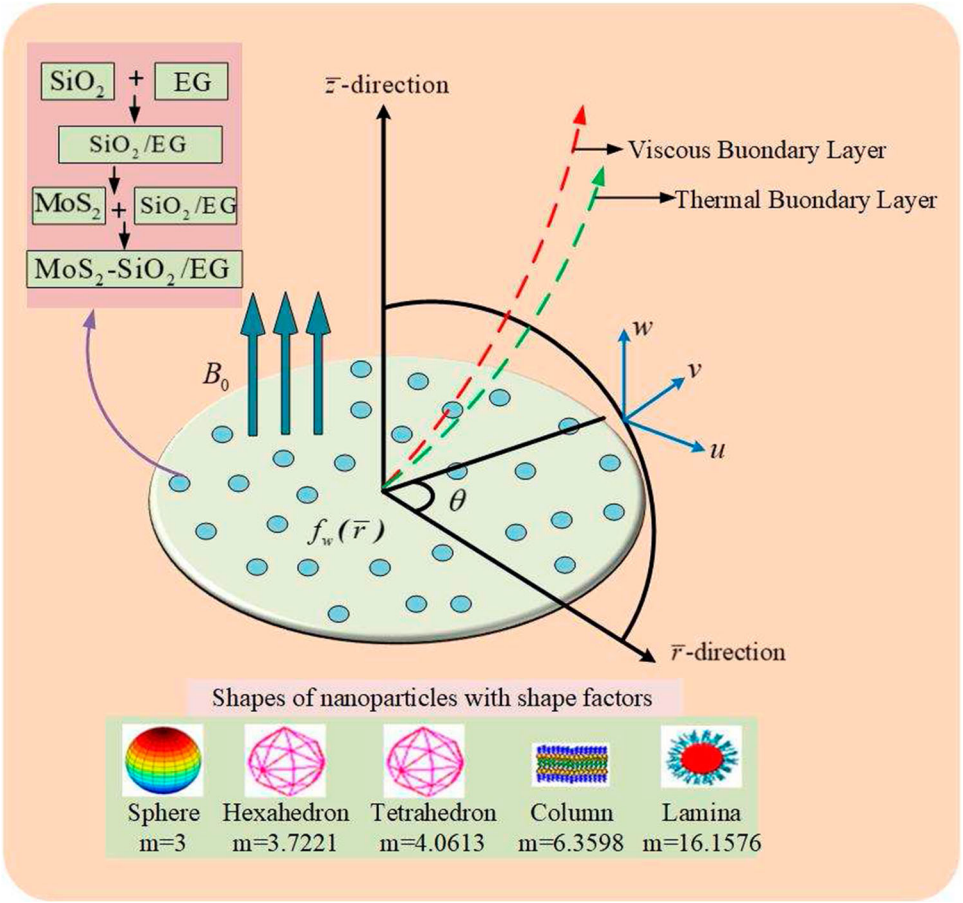

Fig. 1 Physical demonstration of MoS_2–SiO_2/EG flow

Table 1 Numerical values of nanoparticles and base fluid

Thermophysical properties	SiO_2	MoS_2	EG
Density: ρ (kg/m^3)	2650	5060	1113.5
Thermal conductivity: k (W/m K)	1.5	34.5	0.253
Specific heat: c_p (J/kg K)	730	397.746	2430

in Fig. 2. Moreover, thermo-physical properties of ethylene glycol, SiO_2 and MoS_2 are listed in Table 1.

Similarity transformations as well as dimensionless variable ζ and $f(\zeta)$ are accustomed to more assist and simplify the current investigation.

$$u = c\bar{r}f'(\zeta),\ w = -2\sqrt{c\nu_f}f(\zeta),\quad \zeta = \bar{z}\sqrt{\frac{c}{\nu_f}},\ \theta(\zeta) = \frac{T_f - T}{T_f - T_\infty}. \tag{6}$$

After simplification, system of PDEs Eqs. (2–5) for proposed physical problem is reduced into equivalent transformed system of nonlinear coupled ODEs Eqs. (7–9)

$$\frac{1}{\Omega_1}f''' + 2ff'' - f'^2 - \frac{1}{\Omega_2}M^2 f' = 0, \tag{7}$$

$$\frac{1}{\Omega_3}\frac{k_{hnf}}{k_f}\theta'' + 2Prf\theta' + \lambda\frac{(\rho c_p)_f}{(\rho c_p)_{hnf}} = 0, \tag{8}$$

$$f(0) = S,\ f'(0) = 1,\ \theta'(0) = -Bi\frac{k_f}{k_{hnf}}(1 - \theta(0)),$$

$$f'(\zeta) \to 0,\ \theta(\zeta) \to 0 \text{ as } \zeta \to \infty. \tag{9}$$

in which

$$\Omega_1 = \frac{\nu_f}{\nu_{hnf}} = (1-\phi_1)^{2.5}(1-\phi_2)^{2.5} \times \left[(1-\phi_2)\left\{(1-\phi_1) + \phi_1\left(\frac{\rho_{s_1}}{\rho_f}\right)\right\} + \phi_2\frac{\rho_{s_2}}{\rho_f}\right], \tag{10}$$

$$\Omega_2 = \frac{\rho_{hnf}}{\rho_f} = (1-\phi_2)\left[(1-\phi_1) + \phi_1\left(\frac{\rho_{s_1}}{\rho_f}\right)\right] + \phi_2\frac{\rho_{s_2}}{\rho_f}, \tag{11}$$

$$\Omega_3 = \frac{(\rho c_p)_{hnf}}{(\rho c_p)_f} = (1-\phi_2)\left[(1-\phi_1) + \phi_1\left(\frac{(\rho c_p)_{s_1}}{(\rho c_p)_f}\right)\right] + \phi_2\left(\frac{(\rho c_p)_{s_2}}{(\rho c_p)_f}\right). \tag{12}$$

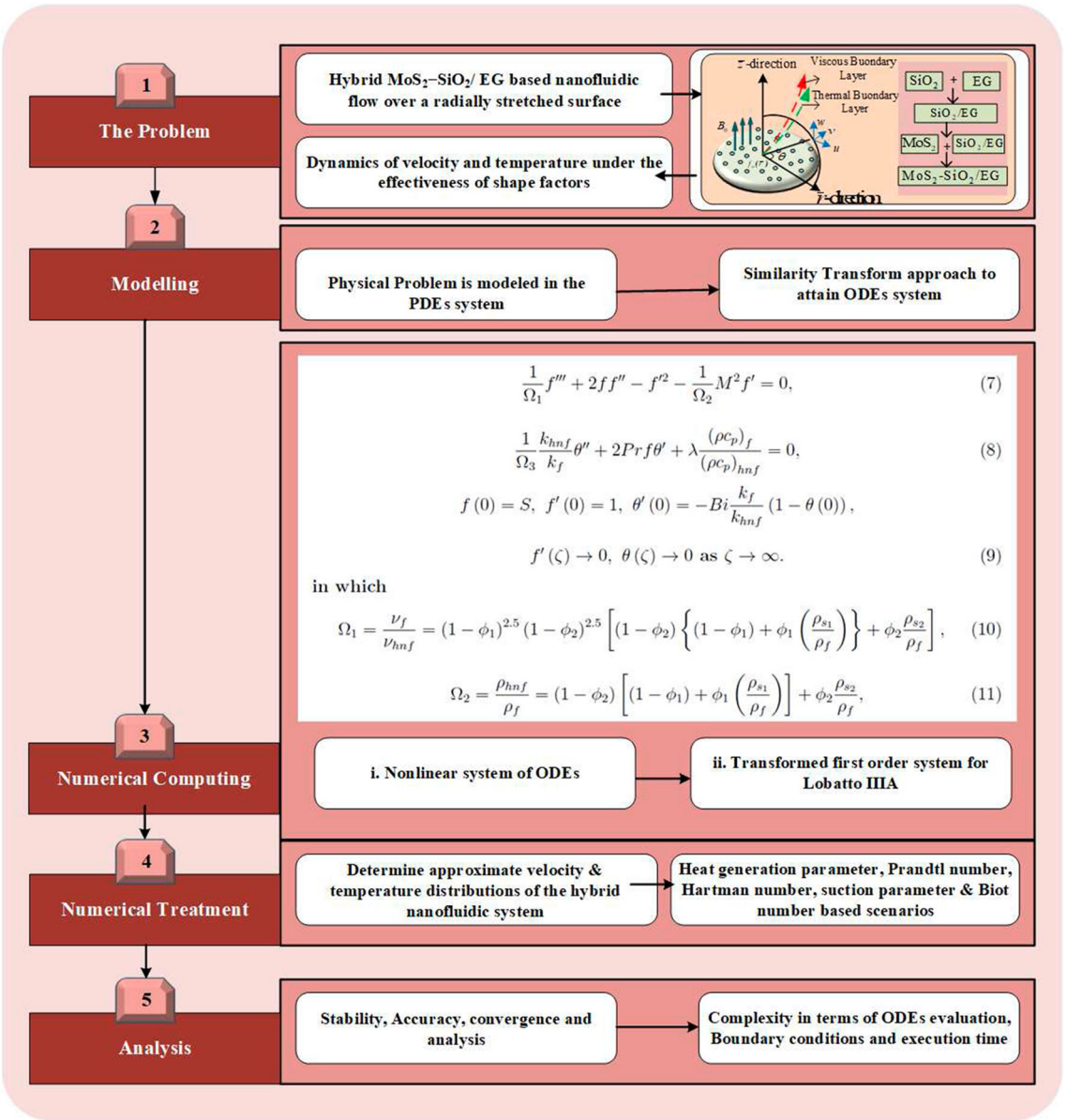

$$\frac{1}{\Omega_1} f''' + 2ff'' - f'^2 - \frac{1}{\Omega_2} M^2 f' = 0, \tag{7}$$

$$\frac{1}{\Omega_3} \frac{k_{hnf}}{k_f} \theta'' + 2Prf\theta' + \lambda \frac{(\rho c_p)_f}{(\rho c_p)_{hnf}} = 0, \tag{8}$$

$$f(0) = S,\ f'(0) = 1,\ \theta'(0) = -Bi \frac{k_f}{k_{hnf}} (1 - \theta(0)),$$

$$f'(\zeta) \to 0,\ \theta(\zeta) \to 0 \text{ as } \zeta \to \infty. \tag{9}$$

in which

$$\Omega_1 = \frac{\nu_f}{\nu_{hnf}} = (1-\phi_1)^{2.5}(1-\phi_2)^{2.5}\left[(1-\phi_2)\left\{(1-\phi_1) + \phi_1\left(\frac{\rho_{s1}}{\rho_f}\right)\right\} + \phi_2 \frac{\rho_{s2}}{\rho_f}\right], \tag{10}$$

$$\Omega_2 = \frac{\rho_{hnf}}{\rho_f} = (1-\phi_2)\left[(1-\phi_1) + \phi_1\left(\frac{\rho_{s1}}{\rho_f}\right)\right] + \phi_2 \frac{\rho_{s2}}{\rho_f}, \tag{11}$$

Fig. 2 Graphical abstract of MoS_2–SiO_2/EG flow

where the condition $f(0) = S$ with $S > 0$ indicates the injection case, while $S < 0$ implies suction.

Furthermore, the dimensionless parameters arising in above set of ODEs, e.g., Hartman number M, heat generation parameter λ, Prandtl number Pr and Biot number Bi, can be defined as

$$M = \frac{\sigma_{\text{hnf}} B_0^2}{c\rho_{\text{f}}},\ \lambda = \frac{Q}{c\left(\rho c_p\right)_{\text{f}}},\ \text{Pr} = \frac{\mu_{\text{f}}\left(c_p\right)_{\text{f}}}{k_{\text{f}}},$$
$$\text{Bi} = h_{\text{f}} k_{\text{f}} \sqrt{\frac{\nu_{\text{f}}}{c}},\ S = \frac{f_{\text{w}}}{2\sqrt{c\nu_{\text{f}}}}. \tag{13}$$

Local Nusselt number $\text{Nu}_{\bar{r}}$ and skin friction coefficient C_{f} are concerned physical quantities, which are defined as

$$Nu_{\bar{r}} = \frac{\bar{r} q_{\text{w}}}{k_{\text{hnf}}\left(T_{\text{w}} - T_{\infty}\right)},\ C_{\text{f}} = \frac{\tau_{\text{w}}}{\frac{1}{2}\rho_{\text{hnf}} u_w^2}. \tag{14}$$

where q_{w} and τ_{w} are

$$q_{\text{w}} = -k_{\text{hnf}} \left(\frac{\partial T}{\partial \bar{z}}\right)\Big|_{\bar{z}=0},$$
$$\tau_{\text{w}} = \mu_{\text{hnf}} \left(\frac{\partial u}{\partial \bar{z}}\right)\Big|_{\bar{z}=0}. \tag{15}$$

In sight of Eq. (6), expression, which is labeled in Eqs. (14) and (15), gives the dimensionless local Nusselt $\text{Nu}_{\bar{r}}$ and skin friction C_{f} as

$$Nu_{\bar{r}} = -\frac{k_{\text{hnf}}}{k_{\text{f}}}\theta'(0)\,,\ C_{\text{f}} = \frac{f''(0)}{(1-\phi)^{2.5}}. \tag{16}$$

where $\text{Nu}_{\bar{r}}$ and C_{f} are reduced Nusselt number and skin friction, respectively.

The system of nonlinear coupled ODEs Eqs. (7–9) is then converted into system of first-order ODEs for Lobatto IIIA. In this investigation, mesh points are fixed at 900, while relative error tolerance varies as 10^{-3}, 10^{-6}, 10^{-9} and 10^{-12}. Approximated velocity and temperature profiles of the hybrid nanofluidic system are determined under consideration of dimensionless quantities, e.g., Hartman number M, heat generation parameter λ, Prandtl number Pr and Biot number Bi-based scenarios. At the end stability, accuracy and convergence analysis are performed.

3 Results and Discussion

In proceeding section, numerically computed impacts for evolving physical constraints on nanofluidic motion and temperature of SiO_2/EG nanofluid and hybridized MoS_2–SiO_2/EG nanofluid are explained. Hartman number M, suction parameter S, nanoparticles volumetric fractions ϕ_1 and ϕ_2, heat absorption/generation parameter λ, Biot number Bi and shape factors m are several influential constraints of interest in this exploration. Graphical and numerical outcomes are designed for both categories of nanofluids to provide comparative study. Dotted curves illustrate outcomes achieved for SiO_2/EG nanofluid, whereas solid curves explain outcomes for hybridized MoS_2–SiO_2/EG nanofluid. For exploration the default numerical values of evolving parameters are presented as: $M = 2.5$, $S = 0.05$, $\lambda = -3$, $m = 3$, $\text{Bi} = 2$, $\text{Pr} = 203.63$, $\phi_1 = 0.01$, $\phi_2 = 0.01$.

Six scenarios each with three cases of the evolving constraints for both nanofluids are shown in Tables 2, 3, 4, 5, 6, 7 and 8. In these tables different values are given to sundry variables in different cases. We have 6 scenarios and 3 cases for each scenario, which demonstrates variation of each parameter. Numerical calculations for different tolerance rates like (10^{-3}, 10^{-6}, 10^{-9} and 10^{-12}) show the adequate accuracy and better convergence obtained by computing scheme. Mesh points used for solutions of each case of 6 scenarios are revealed in Table 2. Table 3 indicates stopping criteria depending on maximum residual obtained for different cases of each scenario, during problem evaluation. Complexity analysis of numerical method Lobatto IIIA to obtain required values of residual error is performed in terms of number of evaluated ODEs and BCs. Number of evaluated ODEs to develop the desired residual is given in Table 4 for different scenarios and cases. The evaluated boundary conditions for the specified accuracy given in Table 3 during different cases of each scenario are presented in Table 5. Table 6 offers skin friction coefficients attained during different cases of sundry scenarios. Nusselt numbers against five different shape factors are calculated for both nanofluids during each case of different scenarios, provided in Tables 7 and 8.

The impacts of suction and magnetic constraints on fluidic motion are displayed in Fig. 3. From Fig. 3a it is determined that suction parameter decelerates flow past of both nanofluids and works as an opposing force. This decreasing trend is caused by the suction taking place at porous stretched surface that interrupts the boundary layer fluid flow and leads to descend fluidic velocity. Similarly rising values of magnetic parameter reduce rate of fluid's flow as can be perceived in Fig. 3b. Existence of magnetic field in directed flows is significant. Moreover, perpendicularly applied magnetic field to the nanofluidic flow direction has dominant effects in opposing manner. Therefore, parameter M acts as a drag force and retards the movement of nanofluids. Deceleration of flow due to suction and magnetic constraints is observed leading for SiO_2/EG nanofluid. Furthermore, in Table- 6 skin friction coefficient which is also termed as velocity gradient rises using positively increasing values of both suction and magnetic constraints.

Biot number (sheet convection) gives influence on nanofluidic velocity and $f(\zeta)$ which is presented in Fig. 4. Nanofluidic flow under up surging values of Biot number possesses ascending behavior, while graphs for $f(\zeta)$ exhibit descending behavior as demonstrated in Fig. 4a, b, respectively. Moreover, leading rise is appeared for hybridized MoS_2–SiO_2/EG nanofluid, while leading drop is found for SiO_2/EG nanofluid.

Figure 5 reveals the effects for volumetric concentrations of SiO_2 and MoS_2–SiO_2 in ethylene glycol on nanofluidic velocity and $f(\zeta)$. It is noticed that a marginal rise in volumes of nanoparticles accelerates the flow and raises the graphs for $f(\zeta)$ as given in Fig. 5a, b, respectively. Since usage of nanoparticles in conventional fluid decreases its viscosity which helps the fluid flow to accelerate. Faster increase in velocity and $f(\zeta)$ is observed for hybridized nanofluid. Furthermore, greater values of ϕ_1 and ϕ_2 increase the skin friction coefficient which is more leading for MoS_2–SiO_2/EG as given in Table 6.

Figures 6, 7 and 8 are plotted to explain the influence of some evolving constraints such as volumetric fractions, Biot number and heat absorption/generation parameter with each against five shape factors on profiles of temperature for both fluids. Sphere, hexahedron, tetrahedron, column and lamina are five considered shapes of nanoparticles. Figure 6 is devoted to inspect the thermal performance of nano and hybrid nanofluid by submerging nanoparticles of both categories up to 5% of volume. Figure 6a, b demonstrates that increasing volume of nanoparticles raises the temperature of both fluids. For hybrid nanofluid 1% volume of

Table 2 Number of mesh points taken for solution of model

Tolerance limits	Scenarios	SiO_2/EG			MoS_2–SiO_2/EG		
		Case-1	Case-2	Case-3	Case-1	Case-2	Case-3
10^{-03}	1	900	900	900	900	900	900
	2	900	900	900	900	900	816
	3	1154	1184	900	1164	1203	900
	4	900	900	900	900	900	900
	5	882	900	900	909	900	900
	6	900	900	900	900	900	900
10^{-06}	1	900	900	900	900	900	900
	2	900	900	1100	900	900	1160
	3	1502	1560	900	1510	1569	900
	4	900	900	900	900	900	900
	5	1422	900	900	1457	900	900
	6	900	900	900	900	900	900
10^{-09}	1	900	900	900	900	900	900
	2	900	900	1125	900	900	1162
	3	1502	1560	900	1510	1569	900
	4	900	900	900	900	900	900
	5	1423	900	900	1457	900	900
	6	900	900	900	900	900	900
10^{-12}	1	900	900	900	900	900	900
	2	900	900	1125	900	900	1162
	3	1502	1560	900	1510	1569	900
	4	900	900	900	900	900	900
	5	1423	900	900	1457	900	900
	6	900	900	900	900	900	900

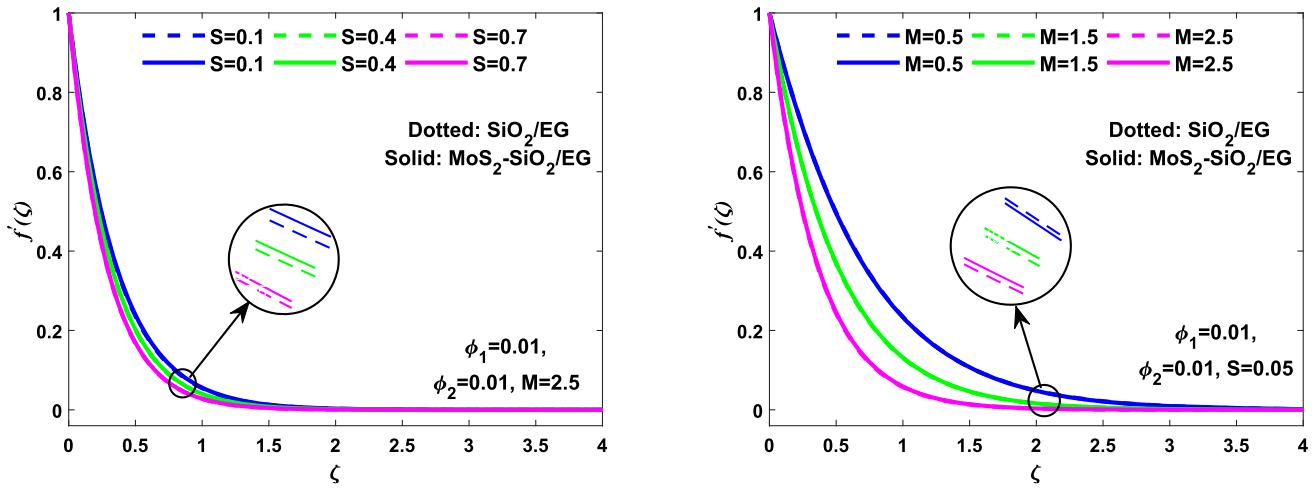

(a) Influence of S on $f'(\zeta)$ **(b)** Influence of M on $f'(\zeta)$

Fig. 3 Influence of suction and magnetic parameters on $f'(\zeta)$

Table 3 Maximum residual during different scenarios and cases of model

Tolerance limits	Scenarios	SiO_2/EG			MoS_2–SiO_2/EG		
		Case-1	Case-2	Case-3	Case-1	Case-2	Case-3
10^{-03}	1	7.87E−06	9.30E−06	1.10E−05	1.01E−05	1.60E−05	2.47E−05
	2	1.38E−05	1.83E−04	6.38E−04	1.75E−05	2.29E−04	2.74E−07
	3	5.82E−05	1.10E−06	7.87E−06	7.25E−05	1.87E−06	1.01E−05
	4	3.75E−04	4.29E−04	4.62E−04	3.91E−04	4.47E−04	4.83E−04
	5	1.62E−08	4.62E−04	2.31E−04	1.56E−08	4.83E−04	2.41E−04
	6	4.62E−04	4.76E−04	4.92E−04	2.00E−04	2.24E−04	2.44E−04
10^{-06}	1	2.49E−08	2.86E−08	3.26E−08	3.12E−08	4.79E−08	7.11E−08
	2	4.18E−08	4.57E−07	1.73E−08	5.21E−08	5.59E−07	1.71E−08
	3	1.49E−09	2.35E−09	2.49E−08	1.50E−09	2.35E−09	3.12E−08
	4	5.33E−07	6.89E−07	8.06E−07	5.50E−07	7.07E−07	8.28E−07
	5	1.57E−08	8.06E−07	3.79E−07	1.51E−08	8.28E−07	3.97E−07
	6	8.06E−07	8.05E−07	8.06E−07	3.33E−07	3.84E−07	4.27E−07
10^{-09}	1	2.49E−11	2.86E−11	3.26E−11	3.12E−11	4.79E−11	7.11E−11
	2	4.18E−11	4.57E−10	6.24E−11	5.21E−11	5.59E−10	5.99E−11
	3	2.09E−12	6.48E−12	2.49E−11	2.11E−12	6.50E−12	3.12E−11
	4	5.33E−10	6.89E−10	8.06E−10	5.50E−10	7.07E−10	8.28E−10
	5	2.07E−11	8.06E−10	3.79E−10	1.91E−11	8.28E−10	3.97E−10
	6	8.06E−10	8.05E−10	8.06E−10	3.33E−10	3.84E−10	4.27E−10
10^{-12}	1	2.49E−14	2.86E−14	3.26E−14	3.12E−14	4.79E−14	7.11e−14
	2	4.18E−14	4.57E−13	6.24E−14	5.21E−14	5.59E−13	5.99E−14
	3	2.09E−15	6.48E−15	2.49E−14	2.11E−15	6.50E−15	3.12E−14
	4	5.33E−13	6.89E−13	8.06E−13	5.50E−13	7.07E−13	8.28E−13
	5	2.07E−14	8.06E−13	3.79E−13	1.91E−14	8.28E−13	3.97E−13
	6	8.06E−13	8.05E−13	8.06E−13	3.33E−13	3.84E−13	4.27E−13

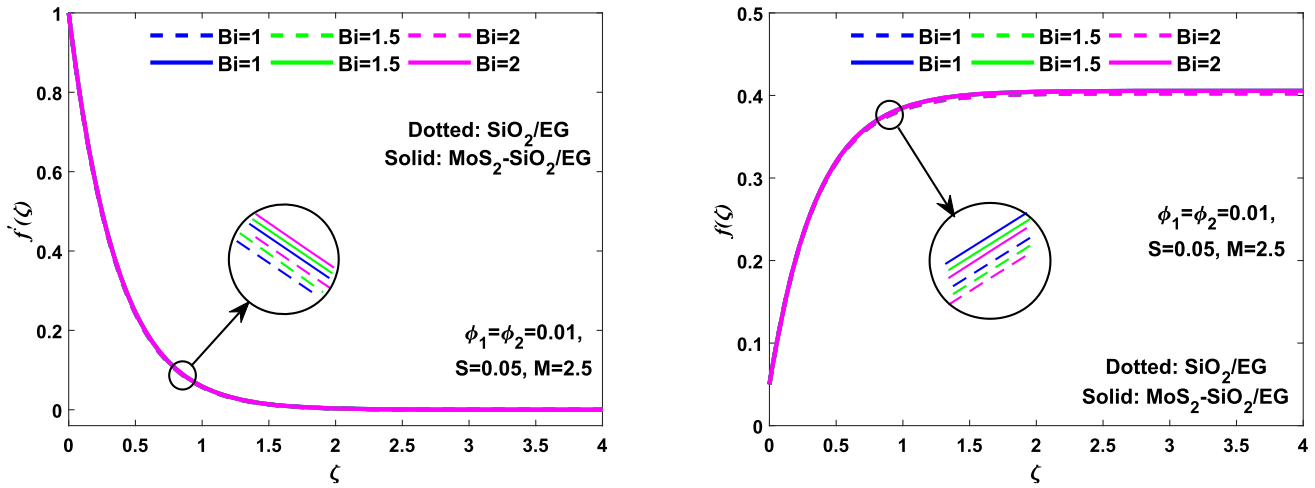

(a) Influence of Bi on $f'(\zeta)$ **(b)** Influence of Bi on $f(\zeta)$

Fig. 4 Influence of Biot number on $f'(\zeta)$ and $f(\zeta)$

Table 4 Number of evaluated ODEs during solution of model

Tolerance limits	Scenarios	SiO_2/EG			MoS_2–SiO_2/EG		
		Case-1	Case-2	Case-3	Case-1	Case-2	Case-3
10^{-03}	1	19,796	19,796	19,796	19,796	19,796	19,796
	2	19,796	19,796	19,796	19,796	19,796	28,768
	3	41,486	32,816	19,796	41,596	33,025	19,796
	4	19,796	19,796	19,796	19,796	19,796	19,796
	5	29,494	19,796	19,796	29,791	19,796	19,796
	6	19,796	19,796	19,796	19,796	19,796	19,796
10^{-06}	1	19,796	19,796	19,796	19,796	19,796	19,796
	2	19,796	19,796	31,892	19,796	19,796	32,552
	3	48,317	40,071	19,796	48,421	40,188	19,796
	4	19,796	19,796	19,796	19,796	19,796	19,796
	5	35,434	19,796	19,796	35,819	19,796	19,796
	6	19,796	19,796	19,796	19,796	19,796	19,796
10^{-09}	1	19,796	19,796	19,796	19,796	19,796	19,796
	2	19,796	19,796	34,416	19,796	19,796	34,897
	3	54,323	40,071	19,796	54,459	40,188	19,796
	4	19,796	19,796	19,796	19,796	19,796	19,796
	5	38,290	19,796	19,796	38,732	19,796	19,796
	6	19,796	19,796	19,796	19,796	19,796	19,796
10^{-12}	1	19,796	19,796	19,796	19,796	19,796	19,796
	2	19,796	19,796	51,286	19,796	19,796	45,353
	3	54,323	43,190	19,796	54,459	43,325	19,796
	4	19,796	19,796	19,796	19,796	19,796	19,796
	5	38,290	19,796	19,796	38,732	19,796	19,796
	6	19,796	19,796	19,796	19,796	19,796	19,796

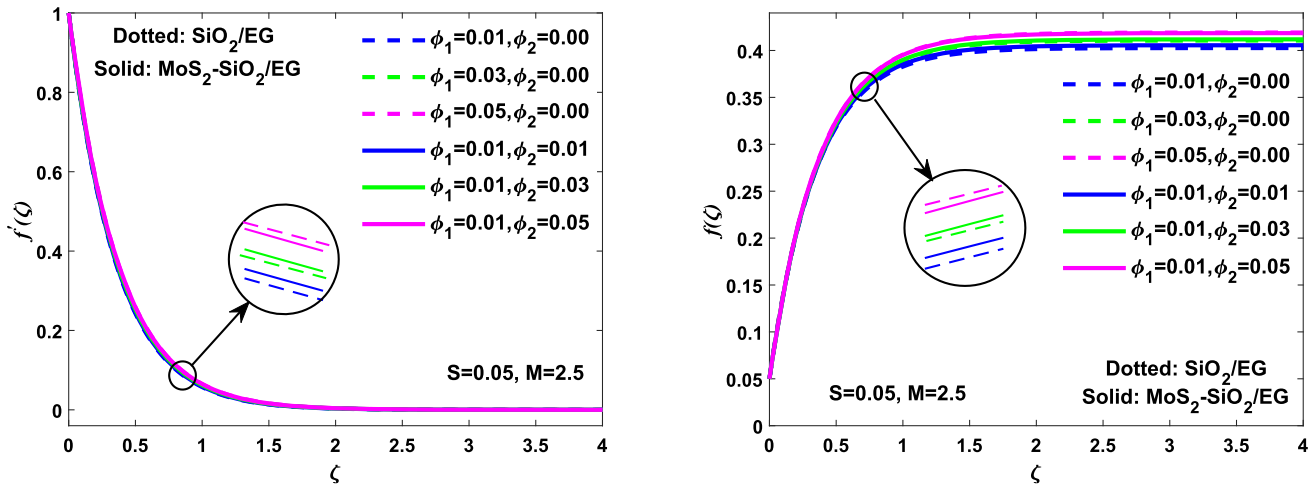

(a) Influence of ϕ_1 & ϕ_2 on $f'(\zeta)$ **(b)** Influence of ϕ_1 & ϕ_2 on $f(\zeta)$

Fig. 5 Influence of volumetric fractions on $f'(\zeta)$ and $f(\zeta)$

Table 5 Number of evaluated BCs during solution of model

Tolerance limits	Scenarios	SiO_2/EG			MoS_2–SiO_2/EG		
		Case-1	Case-2	Case-3	Case-1	Case-2	Case-3
10^{-03}	1	39	39	39	39	39	39
	2	39	39	39	39	39	56
	3	86	56	39	86	56	39
	4	39	39	39	39	39	39
	5	56	39	39	56	39	39
	6	39	39	39	39	39	39
10^{-06}	1	39	39	39	39	39	39
	2	39	39	56	39	39	56
	3	87	57	39	87	57	39
	4	39	39	39	39	39	39
	5	56	39	39	56	39	39
	6	39	39	39	39	39	39
10^{-09}	1	39	39	39	39	39	39
	2	39	39	57	39	39	57
	3	89	57	39	89	57	39
	4	39	39	39	39	39	39
	5	57	39	39	57	39	39
	6	39	39	39	39	39	39
10^{-12}	1	39	39	39	39	39	39
	2	39	39	77	39	39	74
	3	89	58	39	89	58	39
	4	39	39	39	39	39	39
	5	57	39	39	57	39	39
	6	39	39	39	39	39	39

Table 6 Skin friction numbers $-C_f$ for both nanofluids of model

Scenarios	SiO_2/EG			MoS_2–SiO_2/EG		
	$\phi_1 = 0.01$	$\phi_1 = 0.03$	$\phi_1 = 0.05$	$\phi_2 = 0.01$	$\phi_2 = 0.03$	$\phi_2 = 0.05$
$S = 0.1$	2.8981	3.0498	3.2128	2.9467	3.1025	3.2702
$S = 0.4$	3.2336	3.4029	3.5849	3.2947	3.469	3.6564
$S = 0.7$	3.6006	3.7891	3.9917	3.6757	3.8701	4.0793
$M = 0.5$	1.3514	1.4221	1.4981	1.3894	1.4628	1.5419
$M = 1.5$	1.979	2.0826	2.194	2.0187	2.1255	2.2404
$M = 2.5$	2.8453	2.9942	3.1543	2.892	3.045	3.2095

Table 7 Nusselt numbers Nu for nanofluid of model

Scenarios	SiO_2/EG				
	$m = 3.00$	$m = 3.7221$	$m = 4.0613$	$m = 6.3598$	$m = 16.1576$
$Bi = 1.0$	0.6764	0.6749	0.6743	0.6712	0.6656
$Bi = 1.5$	0.878	0.8762	0.8755	0.8716	0.8647
$Bi = 2.0$	1.0319	1.0298	1.029	1.0246	1.0168
$\lambda = 1.5$	0.928	0.9262	0.9254	0.9215	0.9145
$\lambda = 3.0$	1.0319	1.0298	1.029	1.0246	1.0168
$\lambda = 4.5$	1.1025	1.1003	1.0993	1.0946	1.0862

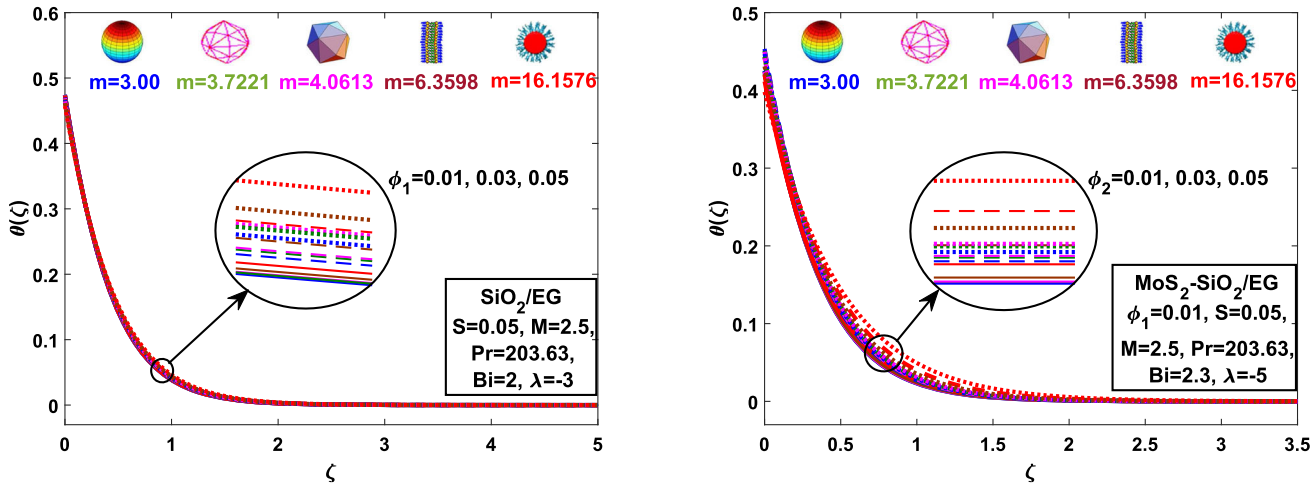

(a) For SiO_2/EG **(b)** For $MoS_2 - SiO_2/EG$

Fig. 6 Influence of volumetric fractions on $\theta(\zeta)$ against m

SiO_2 nanoparticles is reserved fix. Moreover, both nanofluids holding lamina shape of nanoparticles offer maximum temperature for variation of ϕ_1 and ϕ_2. On comparing Fig. 6a, b, it is also visualized that the temperature of hybrid nanofluid leads the temperature of nanofluid.

Thermal behavior of nano and hybrid nanofluid subject to rising sheet convection constraint is pictured in Fig. 7. Biot number (sheet convection) is defined as a quotient of heat transmission resistances within and above the conductive surface that measures the temperature difference by means of applied thermal gradient over the conductive surface. Therefore, upsurge in this quotient raises the temperature curves for both SiO_2/EG and MoS_2–SiO_2/EG nanofluids. Moreover, high temperature is measured by submerging nanoparticles with lamina shape into the both fluid categories. Tables 7 and 8 validate that Nusselt numbers for both fluids are increased using greater values of Bi while decreased using greater values of shape factors.

Impressions of heat absorption/generation constraint on temperature curves are provided in Fig. 8. Since $\lambda < 0$ is heat absorption case, so descending λ values decrease the temperature graphs as well. This behavior is perceived for both SiO_2/EG and MoS_2–SiO_2/EG nanofluids. Lowest temperature is achieved for spherical nanoparticles. In Tables 7 and 8, it is witnessed that Nusselt numbers for both fluids are increased using smaller values of λ while decreased using greater values of shape factors.

4 Conclusion

In this work, a novel approach is presented to numerically examine the nanofluidic and hybrid nanofluidic systems MoS_2–SiO_2/EG, through designed computing scheme. In the proposed model, axisymmetric flow of SiO_2/EG nanofluid as well as MoS_2–SiO_2/EG hybrid nanofluid over a radially stretched disk under influential impacts of magnetic field, suction, internal heat absorption/generation, sheet convection and volumetric fractions is investigated in detail. The foremost judgments of presented work are:

- It is determined that MoS_2–SiO_2/EG hybrid nanofluid holds better thermal abilities because its temperature upsurges more rapidly with rising Biot number and volume fractions as matched to SiO_2/EG nanofluid.
- High magnetic field and suction of porous disk decelerate flow past both nanofluids inside the boundary; on the other hand, volumetric fractions accelerate it.
- Lowest nondimensional temperature is witnessed for nanoparticles of sphere shape, whereas peak temperature is perceived for lamina shape.
- In case of heat absorption constraint, negative impacts on thermal performance of both nanofluids are observed.
- Skin friction coefficient of both nanofluids gain rises, when subject to the influence of suction, magnetic and volumetric fraction constraints and leads in hybrid nanofluidic case.
- Constraints of heat absorption and sheet convection raise the Nusselt number of both nanofluidic categories, but shape factors are a cause to decrease its values.

In future, one may exploit artificial intelligence-based numerical computing paradigm [40–43] for dynamical analysis of hybrid nanoparticles (MoS_2–SiO_2, TiO_2–CuO) on the fluid toward stretched surfaces with the influential impacts of evolving constraints such as slip condition, nanoparticles

Table 8 Nusselt numbers Nu for hybrid nanofluid of model

Scenarios	MoS_2–SiO_2/EG				
	$m = 3.00$	$m = 3.7221$	$m = 4.0613$	$m = 6.3598$	$m = 16.1576$
Bi = 1.0	0.6595	0.6543	0.6519	0.6375	0.5918
Bi = 1.5	0.8572	0.8507	0.8478	0.8299	0.773
Bi = 2.0	1.0083	1.0009	0.9976	0.9773	0.9128
$\lambda = 1.5$	0.907	0.9004	0.8974	0.8793	0.8215
$\lambda = 3.0$	1.0083	1.0009	0.9976	0.9773	0.9128
$\lambda = 4.5$	1.0769	1.069	1.0654	1.0436	0.9739

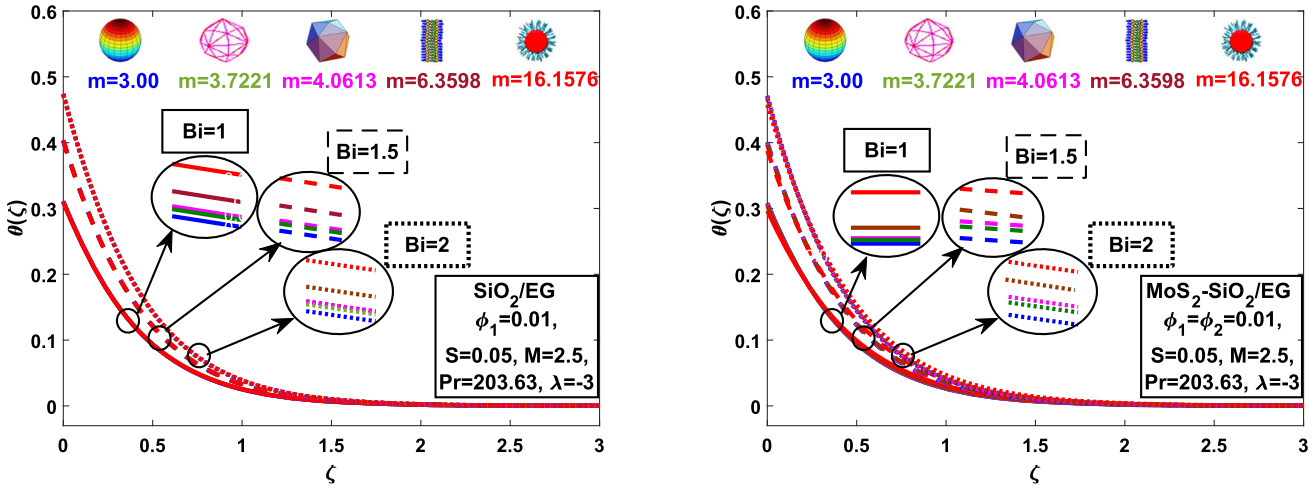

(a) For SiO_2/EG **(b)** For $MoS_2 - SiO_2/EG$

Fig. 7 Influence of Biot number on $\theta(\zeta)$ against m

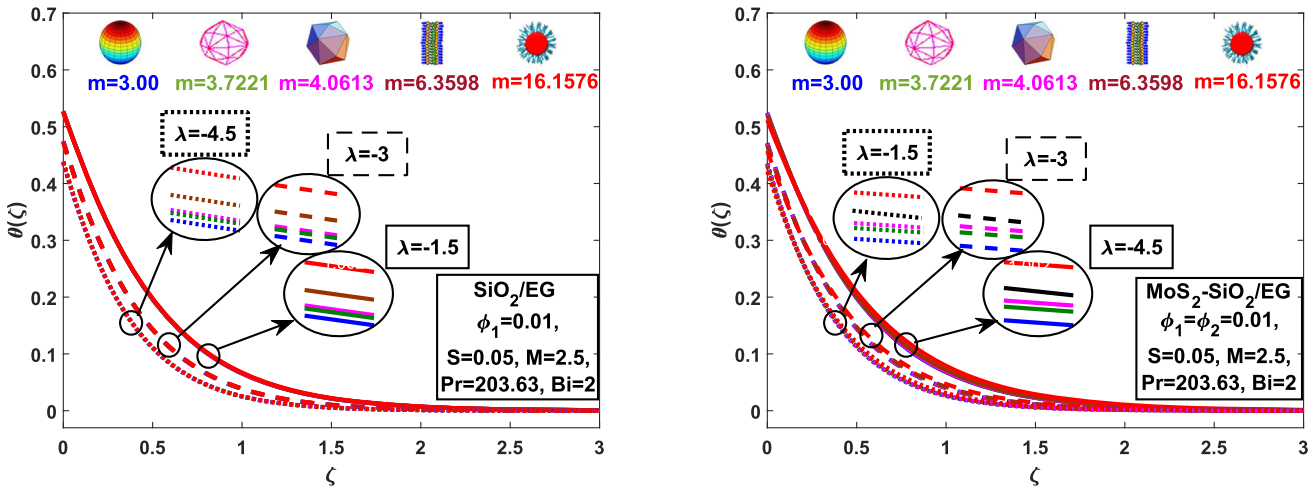

(a) For SiO_2/EG **(b)** For $MoS_2 - SiO_2/EG$

Fig. 8 Influence of parameter λ on $\theta(\zeta)$ against m

shape factors, heat generation, thermal radiation and applied transverse magnetic field.

Funding Open access funding provided by Università degli Studi di Palermo within the CRUI-CARE Agreement.

Declarations

Conflict of Interest The authors declare that there is no conflict of interest, in any aspect.

References

1. Ouyang, C.; Akhtar, R.; Raja, M.A.Z.; Touseef Sabir, M.; Awais, M.; Shoaib, M.: Numerical treatment with Lobatto IIIA technique for radiative flow of MHD hybrid nanofluid (Al2O3-Cu/H2O) over a convectively heated stretchable rotating disk with velocity slip effects. AIP Adv. **10**(5), 055122 (2020)
2. Ahmadi, K.; Khanmohammadi, S.; Khanmohammadi, S.; Bahiraei, M.; Bach, Q.V.: Heat transfer assessment of turbulent nanofluid flow in a circular pipe fitted with elliptical-cut twisted tape inserts. J. Therm. Anal. Calorim. **147**, 727–740 (2020)
3. Ali, M.; Sahito, M.F.; Jha, N.K.; Memon, S.; Keshavarz, A.; Iglauer, S.; Saeedi, A.; Sarmadivaleh, M.: Effect of nanofluid on CO_2-wettability reversal of sandstone formation; implications for CO_2 geo-storage. J. Colloid Interface Sci. **559**, 304–312 (2020)
4. Narla, V.K.; Tripathi, D.; Beg, O.A.: Analysis of entropy generation in biomimetic electroosmotic nanofluid pumping through a curved channel with joule dissipation. Therm. Sci. Eng. Prog. **15**, 100424 (2020)
5. Muhammad, T.; Waqas, H.; Manzoor, U.; Farooq, U.; Rizvi, Z.F.: On doubly stratified bioconvective transport of Jeffrey nanofluid with gyrotactic motile microorganisms. Alex. Eng. J. **61**(2), 1571–1583 (2022)
6. Sheikholeslami, M.; Said, Z.; Jafaryar, M.: Hydrothermal analysis for a parabolic solar unit with wavy absorber pipe and nanofluid. Renew. Energy **188**, 922–932 (2022)
7. Sheikholeslami, M.; Ebrahimpour, Z.: Thermal improvement of linear Fresnel solar system utilizing Al_2O_3-water nanofluid and multi-way twisted tape. Int. J. Therm. Sci. **176**, 107505 (2022)
8. Li, J.; Zuo, W.; Jiaqiang, E.; Zhang, Y.; Li, Q.; Sun, K.; Zhou, K.; Zhang, G.: Multi-objective optimization of mini U-channel cold plate with SiO_2 nanofluid by RSM and NSGA-II. Energy **242**, 123039 (2022)
9. Oke, A.S.; Combined effects of Coriolis force and nanoparticle properties on the dynamics of gold-water nanofluid across nonuniform surface. ZAMM-J. Appl. Math. Mech./Z. Angew. Math. Mechanik. https://doi.org/10.1002/zamm.202100113
10. Junankar, A.A.; Purohit, J.K.; Bhende, N.V.: A review on hybrid nanofluid: current research and sustainable development for turning operation. Int. J. Environ. Sustain. Dev. **21**(1–2), 97–115 (2022)
11. Wang, J.; Xu, Y.P.; Qahiti, R.; Jafaryar, M.; Alazwari, M.A.; Abu-Hamdeh, N.H.; Issakhov, A.; Selim, M.M.: Simulation of hybrid nanofluid flow within a microchannel heat sink considering porous media analyzing CPU stability. J. Petrol. Sci. Eng. **208**, 109734 (2022)
12. Algehyne, E.A.; El-Zahar, E.R.; Elhag, S.H.; Bayones, F.S.; Nazir, U.; Sohail, M.; Kumam, P.: Investigation of thermal performance of Maxwell hybrid nanofluid boundary value problem in vertical porous surface via finite element approach. Sci. Rep. **12**(1), 1–12 (2022)
13. Khan, D.; Kumam, P.; Khan, I.; Khan, A.; Watthayu, W.; Arif, M.: Scientific investigation of a fractional model based on hybrid nanofluids with heat generation and porous medium: applications in the drilling process. Sci. Rep. **12**(1), 1–13 (2022)
14. Ju-Nam, Y.; Lead, J.R.: Manufactured nanoparticles: an overview of their chemistry, interactions and potential environmental implications. Sci. Total Environ. **400**(1–3), 396–414 (2008)
15. Oke, A.S.: Heat and mass transfer in 3D MHD flow of EG-based ternary hybrid nanofluid over a rotating surface. Arab. J. Sci. Eng. (2022). https://doi.org/10.1007/s13369-022-06838-x
16. Wang, A.; Wang, C.; Fu, L.; Wong-Ng, W.; Lan, Y.: Recent advances of graphitic carbon nitride-based structures and applications in catalyst, sensing, imaging, and LEDs. Nano-micro Lett. **9**(4), 1–21 (2017)
17. Lai, C.S.; Jia, Y.; Lai, L.L.; Xu, Z.; McCulloch, M.D.; Wong, K.P.: A comprehensive review on large-scale photovoltaic system with applications of electrical energy storage. Renew. Sustain. Energy Rev. **78**, 439–451 (2017)
18. Sun, T.C.; Uddin, I.; Raja, M.A.Z.; Shoaib, M.; Ullah, I.; Jamshed, W.; Islam, S.: Numerical investigation of thin-film flow over a rotating disk subject to the heat source and nonlinear radiation: Lobatto IIIA approach. Waves Random Complex Media (2022). https://doi.org/10.1080/17455030.2022.2026526
19. Ali, R.; Shahzad, A.; us Saher, K.; Elahi, Z.; Abbas, T.: The thin film flow of Al_2O_3 nanofluid particle over an unsteady stretching surface. Case Stud. Therm. Eng. **29**, 101695 (2022)
20. Qayyum, M.; Ismail, F.; Ali Shah, S.I.; Sohail, M.; El-Zahar, E.R.; Gokul, K.C.; An application of homotopy perturbation method to fractional-order thin film flow of the Johnson–Segalman fluid model. Math. Probl. Eng. **2022**, 1019810 (2022). https://doi.org/10.1155/2022/1019810
21. Chen, Y.; Hong, Z.; Fan, Y.; Lai, T.: Dependence of adhesion force on contact time due to water thin-film flow revealed with an AFM cantilever at low humidity. J. Adhes. Sci. Technol. **36**(6), 620–631 (2022)
22. Siddiqui, A.M.; Mahmood, R.; Ghori, Q.K.: Thin film flow of a third grade fluid on a moving belt by He's homotopy perturbation method. Int. J. Nonlinear Sci. Numer. Simul. **7**(1), 7–14 (2006)
23. Ashraf, H.; Parveen, A.; Rehman, H.U.; Asjad, M.I.; Almutairi, B.N.; Almohsen, B.: Analysis of uniform film thickness and stationary points for the thin film flow of Carreau fluid model in the presence of surface tension gradient (2022). https://doi.org/10.21203/rs.3.rs-1221961/v1
24. Alhussain, Z.A.; Tassaddiq, A.: Thin film blood based Casson hybrid nanofluid flow with variable viscosity. Arab. J. Sci. Eng. **47**(1), 1087–1094 (2022)
25. Moyers-Gonzalez, M.; Hewett, J.; Cusack, D.; Kennedy, B.; Sellier, M.: Non-isothermal thin-film flow of a viscoplastic material over topography. Available at SSRN 4001735.
26. Kamis, N.I.; Jiann, L.Y.; Shafie, S.; Khairuddin, T.K.A.; Md Basir, M.F.: Magnetohydrodynamics boundary layer flow of hybrid

nanofluid in a thin-film over an unsteady stretching permeable sheet. J. Nanofluids **11**(1), 74–83 (2022)
27. Ahmad, F.; Gul, T.; Khan, I.; Saeed, A.; Selim, M.M.; Kumam, P.; Ali, I.: MHD thin film flow of the Oldroyd-B fluid together with bioconvection and activation energy. Case Stud. Therm. Eng. **27**, 101218 (2021)
28. Uddin, I.; Ullah, I.; Raja, M.A.Z.; Shoaib, M.; Islam, S.; Muhammad, T.: Design of intelligent computing networks for numerical treatment of thin film flow of Maxwell nanofluid over a stretched and rotating surface. Surf. Interfaces **24**, 101107 (2021)
29. Ahmad, I.; Mukhtar, B.; Kutlu, K.; Ahmad, F.: A simple neuro-heuristic computational intelligence algorithm for thin film flow equation arising in physical models. In: 2017 16th IEEE International Conference on Machine Learning and Applications (ICMLA), pp. 556–561. IEEE (2017)
30. Devi, S.A.; Devi, S.S.U.: Numerical investigation of hydromagnetic hybrid Cu-Al_2O_3/water nanofluid flow over a permeable stretching sheet with suction. Int. J. Nonlinear Sci. Numer. Simul. **17**(5), 249–257 (2016)
31. Sheikholeslami, M.; Abelman, S.; Ganji, D.D.: Numerical simulation of MHD nanofluid flow and heat transfer considering viscous dissipation. Int. J. Heat Mass Transf. **79**, 212–222 (2014)
32. Kotha, G.; Kolipaula, V.R.; Venkata Subba Rao, M.; Penki, S.; Chamkha, A.J.: Internal heat generation on bioconvection of an MHD nanofluid flow due to gyrotactic microorganisms. Eur. Phys. J. Plus **135**(7), 1–19 (2020)
33. Oke, A.S.: Coriolis effects on MHD flow of MEP fluid over a non-uniform surface in the presence of thermal radiation. Int. Commun. Heat Mass Transf. **129**, 105695 (2021)
34. Hazarika, S.; Ahmed, S.; Chamkha, A.J.: Investigation of nanoparticles Cu, Ag and Fe_3O_4 on thermophoresis and viscous dissipation of MHD nanofluid over a stretching sheet in a porous regime: a numerical modeling. Math. Comput. Simul. **182**, 819–837 (2021)
35. Ijaz, M.; Ayub, M.: Simulation of magnetic dipole and dual stratification in radiative flow of ferromagnetic Maxwell fluid. Heliyon **5**(4), e01465 (2019)
36. Reza, J.; Mebarek-Oudina, F.; Makinde, O.D.: MHD slip flow of Cu-Kerosene nanofluid in a channel with stretching walls using 3-stage Lobatto IIIA formula. Defect Diffus. Forum **387**, 51–62 (2018)
37. Oke, A.S.; Animasaun, I.L.; Mutuku, W.N.; Kimathi, M.; Shah, N.A.; Saleem, S.: Significance of Coriolis force, volume fraction, and heatsource/sink on the dynamics of water conveying 47 nm alumina nanoparticles over a uniform surface. Chin. J. Phys. **71**, 716–727 (2021)
38. Uddin, I.; Akhtar, R.; Zhiyu, Z.; Islam, S.; Shoaib, M.; Raja, M.A.Z.: Numerical treatment for Darcy–Forchheimer flow of Sisko nanomaterial with nonlinear thermal radiation by Lobatto IIIA technique. Math. Problems Eng. 2019.
39. Ahmad, F.; Waqas, H.; Ayed, H.; Hussain, S.; Farooq, S.; Khan, S.A.; Almatroud, A.O.: Numerical treatment with Lobatto-IIIa scheme magneto-thermo-natural convection flow of casson nanofluid (MoS2-Cu/SA) configured by a stretching cylinder in porous medium with multiple slips. Case Stud. Thermal Eng. **26**, 101132 (2021)
40. Faisal, F.; Shoaib, M.; Raja, M.A.Z.: A new heuristic computational solver for nonlinear singular Thomas–Fermi system using evolutionary optimized cubic splines. Eur. Phys. J. Plus **135**(1), 55 (2020)
41. Ahmad, I.; Ilyas, H.; Urooj, A.; Aslam, M.S.; Shoaib, M.; Raja, M.A.Z.: Novel applications of intelligent computing paradigms for the analysis of nonlinear reactive transport model of the fluid in soft tissues and microvessels. Neural Comput. Appl. **31**(12), 9041–9059 (2019)
42. Waseem, W.; Sulaiman, M.; Islam, S.; Kumam, P.; Nawaz, R.; Raja, M.A.Z.; Farooq, M.; Shoaib, M.: A study of changes in temperature profile of porous FIN model using cuckoo search algorithm. Alex. Eng. J. **59**(1), 11–24 (2020)
43. Bukhari, A.H.; Raja, M.A.Z.; Sulaiman, M.; Islam, S.; Shoaib, M.; Kumam, P.: Fractional neuro-sequential ARFIMA-LSTM for financial market forecasting. IEEE Access **8**, 71326–71338 (2020)